Acta Crystallographica Section D
Biological Crystallography
ISSN 0907-4449

Mitigation of X-ray damage in macromolecular crystallography by submicrometre line focusing

Y. Zou Finfrock,[a] Edward A. Stern,[a]* R. W. Alkire,[b] Joshua J. Kas,[a] Kenneth Evans-Lutterodt,[c] Aaron Stein,[c] Norma Duke,[b] Krzysztof Lazarski[b] and Andrzej Joachimiak[d]

[a]Physics Department, University of Washington, Seattle, WA 98195, USA, [b]Structural Biology Center, Argonne National Laboratory, Argonne, IL 60439, USA, [c]National Synchrotron Light Source, Brookhaven National Laboratory, Upton, NY 11973, USA, and [d]Center for Mechanistic Biology and Biotechnology, Argonne National Laboratory, Argonne, IL 60439, USA

Correspondence e-mail: stern@phys.washington.edu

Received 20 November 2012
Accepted 6 April 2013

PDB References: lysozyme, 4htk; 4htn; 4htq

Reported here are measurements of the penetration depth and spatial distribution of photoelectron (PE) damage excited by 18.6 keV X-ray photons in a lysozyme crystal with a vertical submicrometre line-focus beam of 0.7 μm full-width half-maximum (FWHM). The experimental results determined that the penetration depth of PEs is 5 ± 0.5 μm with a monotonically decreasing spatial distribution shape, resulting in mitigation of diffraction signal damage. This does not agree with previous theoretical predication that the mitigation of damage requires a peak of damage outside the focus. A new improved calculation provides some qualitative agreement with the experimental results, but significant errors still remain. The mitigation of radiation damage by line focusing was measured experimentally by comparing the damage in the X-ray-irradiated regions of the submicrometre focus with the large-beam case under conditions of equal exposure and equal volumes of the protein crystal, and a mitigation factor of 4.4 ± 0.4 was determined. The mitigation of radiation damage is caused by spatial separation of the dominant PE radiation-damage component from the crystal region of the line-focus beam that contributes the diffraction signal. The diffraction signal is generated by coherent scattering of incident X-rays (which introduces no damage), while the overwhelming proportion of damage is caused by PE emission as X-ray photons are absorbed.

1. Introduction

Radiation damage is a limiting factor in macromolecular crystallography because it constrains various aspects of X-ray diffraction experiments (obtaining complete data sets from small crystals, for large macromolecular assemblies and for weakly diffracting crystals and for structure phasing, as well as impacting the chemical interpretation of the structure). It also limits the use of continuously improving synchrotron sources in biological research. A practical method to mitigate it would benefit structural biology and help to better utilize synchrotron radiation in biological research. A number of approaches have been proposed and tried (De la Mora *et al.*, 2011; Warkentin *et al.*, 2013; Borek *et al.*, 2010; Bourenkov & Popov, 2010; Finfrock *et al.*, 2010; Garman & Weik, 2011; Kmetko *et al.*, 2011; Sanishvili *et al.*, 2011). One of the strategies is based on a method suggested by Nave & Hill (2005), namely to separate in space the crystal volume where the diffraction signal originates from the crystal volume where radiation damage occurs as much as possible. This is feasible since the dominant primary radiation damage is caused by photoelectrons (PEs) emitted by absorption of the X-rays and it is believed that their damage is typically distributed over micrometre distances at the X-ray energies used in structure

determination and accessible at synchrotrons. Since X-rays from synchrotron sources are typically polarized horizontally and the PEs are preferentially emitted along this direction, the most efficient way to separate their damage is by focusing X-rays to submicrometre vertical line focuses (Stern *et al.*, 2009; Finfrock *et al.*, 2010). We have previously reported, using a 2.3 µm (FWHM) line-focus beam, that the PEs generated in lysozyme crystals by 18.6 keV X-rays travel 1.5 µm on average (Finfrock *et al.*, 2010). This experiment was limited by the precision of the mechanical drive, the dimensions of the line-focus beam and assumptions about the experimental conditions. To estimate PE travel we resorted to a correction procedure. We applied a devolution that assumed a parameterized shape of the PE spatial damage distribution (Finfrock *et al.*, 2010). The values of the parameters were determined by the best fit to the measured data. Using this approach we were able to fit the experimental data reasonably well, but it resulted in underestimation of the PE penetration depth. Here, we report more accurate experiments with a high-precision mechanical system and a submicrometre-width line-focus X-ray beam. Our new measurements have the resolution to directly measure the spatial damage distribution and have substantially improved the estimated PE penetration depth and spatial damage distribution in protein crystals.

2. Experimental

Measurements were performed at the Structural Biology Center (SBC) on the 19-ID beamline at the Advanced Photon Source. The sample investigated was a large (100 × 200 × 700 µm) tetragonal lysozyme crystal (space group $P4_32_12$, unit-cell parameters $a = b = 78.87$, $c = 36.84$ Å) (reference structure PDB entry 1lz8; Dauter *et al.*, 1999) using 18.6 keV X-rays with a single refractive line-focus lens transmitting a flux of 2.7×10^9 photons s^{-1}. The crystal contained 41% solvent including 6.0%(*w*/*v*) NaCl. The protein crystal was cryocooled with liquid nitrogen and for all data-collection experiments it was kept in a dry nitrogen-gas stream at 100 K. The crystal was illuminated with X-rays in two steps: a short 'probing' data set followed by longer exposed 'damage' data set distributed over the same crystal volume. Diffraction patterns were recorded on an ADSC Quantum 315r CCD detector while the sample crystal was kept in a 100 K cryostream flow. The sample-to-detector distance was 250 mm. The crystal diffracted to atomic resolution with a high signal-to-background ratio. Data were processed and scaled with *HKL*-3000 (Minor *et al.*, 2006).

The line-focus lens was fabricated in a [100] single-crystal silicon wafer using microfabrication techniques (Evans-Lutterodt *et al.*, 2003). The lens opening is 34 µm and is about 2 mm long with an elliptical profile etched down perpendicular to the [100] face to a depth of ∼100 µm. The 100 µm depth produces the length of the line focus. Owing to imperfections in the etching process, it is best to avoid using the top and the bottom of the lens vertical line focus. To compensate for beamline optics imperfections, a 12.5 µm horizontal by 10 mm vertical slit was placed about 1 m upstream to act as the new X-ray source. The refractive lens is designed to produce a submicrometre line-focus mini-beam with a 60 mm focal length at 18.6 keV X-ray energy. The alignment of the lens is very sensitive to the vertical rotation axis perpendicular to the X-ray beam, requiring an adjustment within a resolution of ∼0.005° to attain the best focus.

The focused beam profile was characterized with a 30 nm 'thin wire' consisting of a 70 µm wide and 30 nm thick Cr evaporated layer on an elevated 'wall' etched on a silicon wafer and stepping its 30 nm thick layer through the focus with a piezoelectric linear drive at a resolution of about 20 nm per step. An NaI (Tl) scintillation detector was used to measure the Cr fluorescence signal. The measured focused beam profile had an FWHM of 0.70 ± 0.05 µm and was 70 µm tall.

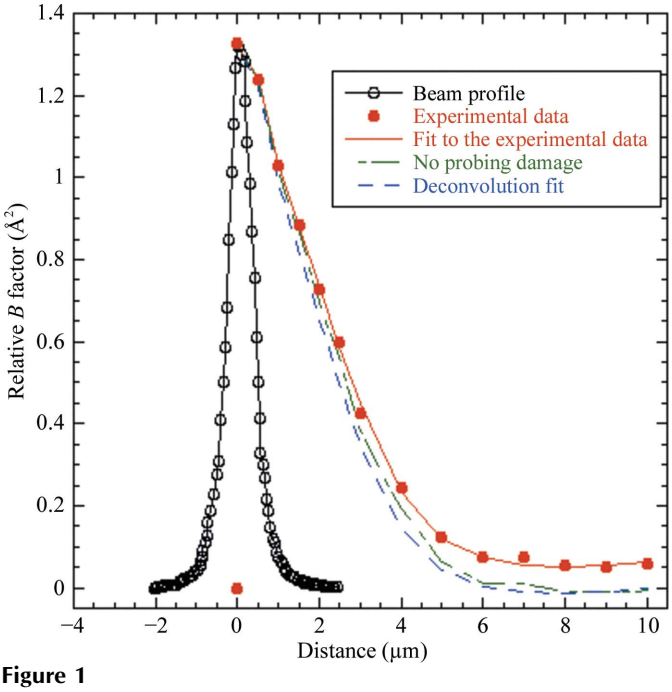

Figure 1
Plots of the measured lens focus profile (black open circles), the spatially dependent damage (red dots) and its fit (red line), the deconvoluted spatially dependent damage (blue dashed line) and the spatially dependent data with the probing damage removed (green short/long dashed line).

3. Measurements and results

3.1. Spatial dependence of PE damage

The standard definition of X-ray dose, as usually calculated using the *RADDOSE* program (Paithankar & Garman, 2010), is not used here since it is not appropriate when mitigation is present, which makes the damage dependent on both dose and mitigation. A different definition is used that is appropriate when mitigation is present: X-ray dose is defined as the total number of X-ray photons incident during exposure of the diffracting crystal volume. The X-ray dose was calculated based on X-ray flux measurements in prior experiments using a dry-nitrogen-filled ionization chamber of active length

100 mm as described previously (Rosenbaum *et al.*, 2006) and corrected for the decline in synchrotron current.

There are two steps in spatially dependent damage measurement using the line-focus lens. Firstly, a probing data set was collected from a fresh crystal with 1.5 s exposure time per image and 0.5° oscillation over a 4° angle range: a dose of 12 s exposure. The crystal was damaged with a dose of exposure time 200 s and the crystal was probed again. After initial probing, the damage/probe sequence was repeated three times for a total dose exposure of 648 s (a total dose of 1.75×10^{12} photons). The damage X-ray exposure was thus 54 times that of a single probe. We used the relative *B* factor between data sets as a measure of the global radiation damage to the protein crystal (Garman, 2010; Holton, 2009; Kmetko *et al.*, 2006, 2011; Warkentin *et al.*, 2011). The relative *B* factor is proportional to the change in the isotropic mean-squared atomic displacements $\Delta(u^2) = B/8\pi^2$. The $\Delta(u^2)$ decreases the intensity of the Bragg spots by the Debye–Waller factor of $\exp(-B/4r_j^2)$ in the r_j resolution shell. The total damage was in the linear range in which the damage measured, as an increase in the relative *B* factor between the data sets, remained proportional to the X-ray dose as determined by our threefold initial damaging and probing sequence and also agrees with Holton (2009). Afterwards, the sample was moved away relative to the damaged crystal volume to probe the spatial dependence of global radiation damage outside the initial highly damaged region. The step size was 0.5 µm from 0 to 3 µm, followed by 1 µm steps from 3 to 10 µm.

Fig. 1 plots the measured focused beam profile together with the measured spatially dependent global damage induced by the initial X-ray dose within the beam profile. The beam profile is calibrated to the *B*-factor scale by setting the maxima of both the profile and the *B* factor at the same point because of the linear relation between *B* factor and dose. The spatial dependence of both the extent and the intensity of the X-ray dose within the focus shapes the profile. In addition, the deconvolution of the spatial damage is plotted, which corrects for the finite width of the focus and for the small cumulative damage caused by probing, thus displaying the spatial damage produced by a line focus of delta-function width. Note that the damage caused by PEs extends beyond the irradiated region by about 5 µm or so. This is called the PE penetration depth. However, there is no sharp cutoff of the damage as a function of distance, adding some uncertainty to the PE penetration depth.

3.2. Mitigation of PE damage

The amount of structural information that can be obtained from a given crystal is limited by radiation damage. A measure of the amount of structural information obtained in an experiment is the diffraction signal, namely the number of diffracted photons, which is proportional to the X-ray dose. The object of using a focused X-ray beam is to mitigate the damage and thus increase the amount of structural information that can be obtained from a given crystal.

Table 1
Focused and unfocused experimental details.

Experiment	Ion-chamber current (A)	Sample dimensions (µm)	Time of exposure (s)	Relative *B* factor (Å^2)
Large beam	0.0064 ($\mathrm{Flux_L}$)	$70 \times 100 \times 300$ ($\mathrm{Vol_L}$)	432.8 (T_L)	0.22 (B_L)
Focused	0.0018 ($\mathrm{Flux_F}$)	$70 \times (5 \pm 0.5) \times 300$ ($\mathrm{Vol_F}$)	648 (T_F)	0.42 (B_F)

Note from Fig. 1 that in a focused-beam experiment much of the damage takes place outside the irradiated region. However, the fact that the crystal has been damaged means that limited further information can be obtained from it. Thus, the region of damage contains both the irradiated region (the beam profile) and the PE-damaged region outside the beam profile. However, only the damage in the X-ray-irradiated region within the beam profile degrades the diffraction signal.

The mitigation of radiation damage is defined as the ratio between the damage sustained by a sample irradiated with focused submicrometre and large beams of the same X-ray dose per unit volume. The focused-beam measurements were performed using the lens apparatus and 12.5 µm slits located upstream. The beam height was determined by a vertical slit, the height of which was adjusted to optimize the sharpness of the focus. For the large-beam measurements the lens apparatus and the 12.5 µm upstream slits were removed and the beam was shaped by a horizontal slit and the same vertical slit. The large-beam shape was measured using a 25 µm tungsten wire and was found to be 70 µm high and 100 µm wide. Thus, the damaged volume in the large-beam case was $70 \times 100 \times 300$ µm (300 µm being the crystal thickness).

The damaged volume in the focused-beam experiment was then 70 µm × 300 µm × the width of the damaged region. For a single line focus the width of the damaged region is the 5 ± 0.5 µm PE penetration depth. The lysozyme diffraction data collection was performed using a fresh portion of the same crystal and using the same experimental procedure as for the focused case except that the exposure time and total photon flux were different. The total absorbed dose is about 5.3×10^6 Gy in the focused case (as calculated using *RADDOSE* Version 2.20; Paithankar & Garman, 2010). The experimental details are shown in Table 1.

To compare global damage of the two cases requires scaling the line-focused beam case to cover the same crystal area as the large-beam case and for both to be irradiated with the same X-ray dose (ion-chamber current). The ion-chamber current measures the flux of X-rays incident on the sample. The ion chamber was calibrated previously. The dose per unit volume (D_L) for an unfocused experiment is given by

$$D_\mathrm{L} = \mathrm{Flux_L}/\mathrm{Vol_L} = 0.0064/(70 \times 100 \times 300) = 3.05 \times 10^{-9}. \quad (1)$$

Since the damage decreases approximately linearly, outside the profile two neighboring line focuses about 5 ± 0.5 µm apart would approximately fully damage the region between them. Only half of each line focus contributes to the damaged sample region between them. Thus, the damaged region per

Table 2
Data-collection and structure-refinement statistics.

Values in parentheses are for the highest resolution shell.

	A	*B*	*C*
Space group	$P4_32_12$	$P4_32_12$	$P4_32_12$
Unit-cell parameters (Å)	$a = b = 78.92$, $c = 36.87$	$a = b = 78.96$, $c = 36.88$	$a = b = 79.02$, $c = 36.91$
Wavelength (Å)	0.6666	0.6666	0.6666
Resolution (Å)	27.91–1.40	27.92–1.30	27.94–1.20
Observed reflections	166458	207860	248889
Unique reflections	23590	29301	37196
$R_{\rm merge}$†	0.080	0.068	0.067
Completeness (%)	99.3 (97.2)	99.2 (96.2)	99.0 (99.8)
Multiplicity	7.1	7.2	6.8
$\langle I\rangle/\langle\sigma(I)\rangle$	20.3 (2.6)	25.6 (3.2)	25.8 (2.7)
Phasing method	MR	MR	MR
$R_{\rm cryst}/R_{\rm free}$‡	0.130/0.163	0.127/0.158	0.136/0.152
Solvent molecules	175	175	175
R.m.s. deviations			
Bond lengths (Å)	0.005	0.015	0.008
Bond angles (°)	0.984	1.518	1.211
Average *B* factor (Å^2)	12.84	12.50	12.31
Ramachandran plot, residues in (%)			
Most favored regions	99.3	99.3	99.3
Additionally allowed regions	0.7	0.7	0.7
PDB code	4htq	4htn	4htk

† $R_{\rm merge} = \sum_{hkl}\sum_i |I_i(hkl) - \langle I(hkl)\rangle|/\sum_{hkl}\sum_i I_i(hkl)$, where $I_i(hkl)$ is the intensity of the *i*th observation of reflection *hkl*. ‡ $R = \sum_{hkl}||F_{\rm obs}| - |F_{\rm calc}||/\sum_{hkl}|F_{\rm obs}|$ for all reflections, where $F_{\rm obs}$ and $F_{\rm calc}$ are observed and calculated structure factors, respectively. $R_{\rm free}$ is calculated analogously for the test reflections, which were randomly selected and excluded from refinement.

line focus is the region between, namely 5 × 70 × 300 µm. The dose per unit volume ($D_{\rm F}$) for a focused experiment is

$$D_{\rm F} = {\rm Flux_F/Vol_F} = 0.0018/[70 \times (5 \pm 0.5) \times 300] = 1.71 \times 10^{-8}. \quad (2)$$

The flux correction factor (F) is given by

$$F = D_{\rm F}/D_{\rm L} = 1.71 \times 10^{-8}/3.05 \times 10^{-9} = 5.61. \quad (3)$$

The exposure-time correction factor T for the X-ray doses is given by

$$T = T_{\rm F}/T_{\rm L} = 648/432.8 = 1.50. \quad (4)$$

Correcting the unfocused experiment *B* factor to the same X-ray dose as the focused experiment,

$$B_{\rm largebeam} = B_{\rm L} \times F \times T = 0.22 \times 5.61 \times 1.50 = 1.85,$$
$$B_{\rm focused} = 0.42. \quad (5)$$

Therefore, the mitigation factor with the line-focused beam is

$$B_{\rm largebeam}/B_{\rm focused} = 4.4 \pm 0.4. \quad (6)$$

3.3. Assessing site radiation damage with a line-focus beam

To assess the site radiation damage, three complete atomic resolution data sets were collected from three fresh sectors of a lysozyme crystal separated by 20 µm at 18.6 keV using a different line-focus beam with a profile of FWHM 1.09 ± 0.07 µm and a height of 70 µm. This beam had a mitigation factor of 2.5. The vertical height of the crystal was smaller than that of the X-ray beam (50 × 100 × 200 µm) and was aligned so that no fresh crystal was exposed to the line beam during data collection. The exposure times were 3 s deg^{-1} for data set *A*, 6 s deg^{-1} for data set *B* and 10 s deg^{-1} for data set *C*, with 1.0–0.5° oscillation over a 90° angle range. The total X-ray dose for each data set was 6.7 × 10^{11} photons for data set *A*, 1.32 × 10^{12} photons for data set *B* and 2.17 × 10^{12} photons for data set *C*. The intensities were integrated and scaled with the *HKL*-3000 program suite (Table 2; Minor *et al.*, 2006). Structures were initially refined using *phenix.refine* (Afonine *et al.*, 2012). Further model building to complete the structure was performed manually using *Coot* (Emsley & Cowtan, 2004). The final refinement was carried out with *PHENIX* (Table 2).

The structures were refined to 1.40, 1.30 and 1.20 Å resolution for data sets *A*, *B* and *C*, respectively. There are four disulfide bridges in lysozyme and they are easily observed at atomic resolution. The disulfide bridges are good indicators of damage because the S atoms have the highest X-ray absorption and scattering cross-section in the structure. It has been reported by a number of investigators that these bridges deteriorate quite readily in lysozyme crystals upon radiation damage (Weik *et al.*, 2000; Shimizu *et al.*, 2007; Wang *et al.*,

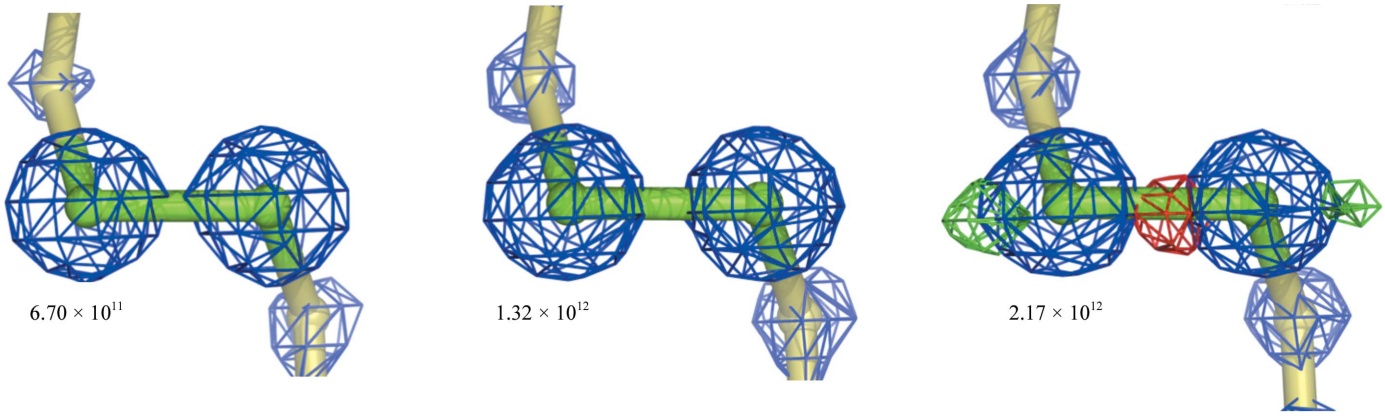

Figure 2
Electron-density maps ($2F_{\rm o} - F_{\rm c}$, blue; $F_{\rm o} - F_{\rm c}$, green for positive and red for negative density) contoured at 3σ for the region near the Cys30–Cys115 disulfide bridge in three lysozyme structures determined from the data obtained with a line-focus beam at three different doses. This is the disulfide bridge with the most visible damage in data set *C*. The total dose of X-ray photons is shown for each data set.

2007; Cianci *et al.*, 2008; Carpentier *et al.*, 2010; Petrova *et al.*, 2010; Borek *et al.*, 2010). The integrity of the lysozyme disulfide bridges was inspected. Fig. 2 shows electron-density maps for the Cys30–Cys115 disulfide bridges of three lysozyme structures determined at three different X-ray doses. This disulfide bridge shows the most visible damage in data set *C*. The highest absorbed dose (5.3×10^6 Gy for data set *C*; calculated with *RADDOSE*, which overestimates the dose by the mitigation factor of 2.5 owing to the escape of PEs) was similar to the dose that the crystal received during our damage experiment and it corresponds to approximately one quarter of the Henderson limit (Henderson, 1990). The middle dose (3.18×10^6 Gy, data set *B*) corresponds to approximately one sixth and the lowest dose (1.59×10^6 Gy, data set *A*) was approximately one twelfth of the Henderson limit. Again, the actual dose is overestimated by the mitigation factor of 2.5. In all three cases the disulfide bridge is intact, with some residual positive electron density indicating that some damage is only observed at the highest dose. Similar behavior is observed for all four disulfide bridges. The occupancy of the S atoms refines to 1, with very comparable *B* factors (7.02–13.84 Å^2) for all atoms and data sets. It has been reported previously that in lysozyme visible radiation damage to disulfide bridges occurs at doses corresponding to one tenth of the Henderson limit (Weik *et al.*, 2000; Shimizu *et al.*, 2007; Cianci *et al.*, 2008; Carpentier *et al.*, 2010). The damage rates are different for all four disulfide bridges and are independent of wavelength. Specific damage to the Cys30–Cys115 disulfide bridge has also been reported (Weik *et al.*, 2000; Shimizu *et al.*, 2007; Cianci *et al.*, 2008; Carpentier *et al.*, 2010). Similar results at atomic resolution have been reported previously for elastase crystals. Significant damage was observed at low doses and when the dose reached the Henderson limit, damage to the disulfide bridges resulted, with the occupancies of sulfur varying from 0.75 to 0.34 (average occupancy of 0.60; Petrova *et al.*, 2010). When the dose was increased further, the occupancy values remained almost unchanged. It has also been reported that at low doses radiation damage is linear with dose (Teng & Moffat, 2002; Sliz *et al.*, 2003; Kmetko *et al.*, 2006; Bourenkov & Popov, 2010; Borek *et al.*, 2010, Finfrock *et al.*, 2010). For lysozyme data collected with a line focus we observe S-atom occupancies of 1, suggesting no damage. Difference electron-density maps showed no damage to disulfide bridges Cys6–Cys127 and Cys64–Cys80, although some residual damage was indicated in data set *C* for Cys30–Cys115 and Cys76–Cys94.

4. Discussion

4.1. PE emission

For a given photon energy, the structural information (diffraction signal) obtained is proportional to the X-ray dose. It is generally assumed that the total amount of damage is proportional to the total amount of energy deposited in the crystal. However, with submicrometre focusing a new phenomenon appears of PE-dependent damage occurring in regions that do not contribute to the diffraction signal, giving a spatial separation between the two. It is this separation that allows the large mitigation factor of ∼4.

In Fig. 1 the separation is visible as the damage occurs outside the beam profile that is depositing the X-ray dose. Fig. 1 shows the measurement of relative *B* factors on the right-hand side of the X-ray beam profile. However, the damage is observed symmetrically on both sides of the beam profile (data not shown). The total damage on the right (positive) side (the volume outside the beam profile plus the volume on the positive side of the profile) is determined by the X-ray dose. However, the damage on the positive side of the profile is only about one quarter of the total damage, while when considering a larger beam case (>50 µm) essentially all of the damage is contained within the irradiated volume and deteriorates the X-ray signal. The use of a submicrometre line-focus beam leads to mitigation of the radiation damage. In general, the mitigation factor is given by the ratio of the total damage area (profile plus PE exterior) divided by the profile area. The total area is determined by the X-ray dose, while the profile is determined by the lens. With a good lens the profile is Gaussian and can be characterized by its FWHM. For a given X-ray dose and energy the mitigation varies as $(\mathrm{FWHM})^{-1}$.

4.2. Spatial damage distribution

We were at first surprised by the shape of the spatial damage distribution since we did not expect a monotonically decreasing shape. Our reasoning was that the damage should initially increase with distance as the PEs slow down and their stopping power (PE energy loss per unit distance) increases, *i.e.* the interaction of the PEs with the protein electrons initially increases and then drops as the PEs lose their energy to the environment (Stern *et al.*, 2009).

To understand the shape of the spatial damage distribution requires a more complete analysis of the physics involved. Synchrotron radiation is strongly polarized in the horizontal direction. When an X-ray photon of the energies employed in macromolecular crystallography is absorbed by a low-*Z* atom such as C, N or O, the emitted PE has an initial angular distribution approximately proportional to $\cos^2\theta \mathrm{d}\Omega$, where $\mathrm{d}\Omega$ is the unit solid angle proportional to $\sin\theta \mathrm{d}\theta$ (Finfrock *et al.*, 2010). Thus, the angular distribution is $\sim\cos^2\theta\sin\theta \mathrm{d}\theta$ and is independent of φ. Here, θ is the initial emission angle between the PE and the polarization directions and φ is the azimuthal angle. The PE initial emission distribution has its maximum at $\theta = 35.3^\circ$, resulting in a preference for PE emission along the X-ray polarization direction (Finfrock *et al.*, 2010).

After emission, the PE begins scattering from its initial direction as it interacts with the surrounding protein and solvent atoms in the crystal. Because the line-focus beam illuminates a planar sheet through the crystal, by symmetry the only variable is the component of the PE path along the polarization direction perpendicular to the sheet. The scattering randomly spreads out the PE path about its initial direction.

A program that includes scattering effects for a given initial direction by a Monte Carlo procedure is *CASINO* (Hovington

& Drouin, 1997), and it has been applied to our case with a modification to allow integration over all initial PE directions. We simulated the energy-loss distribution for a cubic sample with a side length of 20 µm using 100 000 electrons and a stoichiometry taken from our lysozyme sample including 6%(*w*/*v*) NaCl. The electron beam was set to 0.1 µm in diameter with an initial energy of 17.35 keV. The physical models used were as follows. The elastic scattering used data based on *ELSEPA* calculations (Salvat *et al.*, 2005). Inelastic scattering was taken into account using an empirical formula for the stopping power (Joy & Luo, 1989) which is based on a modified Bethe approximation suitable for low-energy electrons. Finally, the distribution was calculated by integrating over the initial angle of the photoelectron with the correct angular weighting.

Fig. 3 shows the results of the *CASINO* calculation integrated over a solid angle with $\cos^2\theta\sin\theta$ weighting along with the experimental results. There is appreciable signal near $x = 0$ coming from electrons initially carrying negative $\overline{x}$ (where $\overline{x}$ is a unit vector along the X-ray polarization direction) momentum. The measured curve has a small cumulative probing damage. Its effect is visible at the longer distances where the damage levels off above zero. In both the *CASINO* calculation and during crystal structure measurements damage caused by probing is not present. Thus, we show the damage after removing the probing damage in both Figs. 1 and 3. The *CASINO* calculation is normalized to have the same area as the experiment so as to calibrate it to the experiment X-ray dose. Note that there is a large discrepancy remaining between *CASINO* theory and measurements. We have tried to understand what could cause this discrepancy but have failed to do so. The fact is that *CASINO* has only qualitative agreement with experiment and thus the theoretical approximations are not quantitatively adequate.

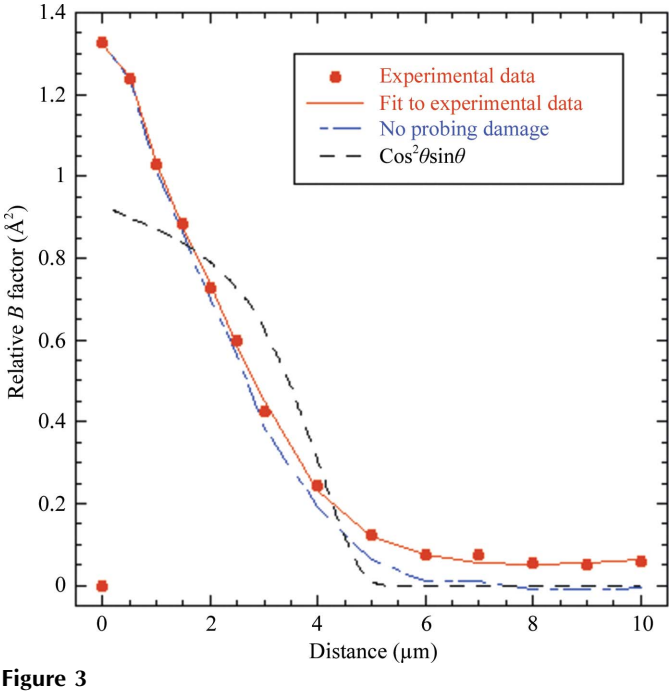

Figure 3
Results of the *CASINO* calculation integrated over a solid angle (black dashed line) compared with the experimental results (red dotted line), the fitted curve (red line) and the fitted curve corrected for damage caused by probing (blue dotted/dashed line) which is not present when the damage is initially deposited.

As discussed in §3.2, the damage in the larger beam case is about four times that of the focused case even though both were exposed to the same X-ray dose per unit volume. This experimental result shows that the submicrometre focused beam is significantly less damaging to the crystal than the larger beam because of the new phenomenon of spatial separation between X-ray dose damage and PE damage.

A recent publication (Sanishvili *et al.*, 2011) provided evidence that micrometre point focusing of X-rays also reduces radiation damage in the irradiation region and has a similar monotonic decrease in the spatial distribution of damage. Our paper discusses the use of submicrometre line focusing, which has advantages over point focusing for fabricating a practical device to mitigate radiation damage and can readily increase the irradiated crystal volume when multi-line lenses are considered (Finfrock *et al.*, 2010; see §5).

5. Design considerations to mitigate damage

Fig. 3 shows that the PE damage at 18.6 keV is contained within 5 µm of the X-ray beam center (and is symmetrically distributed on both sides). Since there is no sharp drop in the PE damage distribution but only a gradual one, there is some uncertainty as to the value that should be assigned to the PE penetration depth. The gradual ending of the PE damage distribution is a result of Monte Carlo scattering of the PEs. In order to collect all of the diffraction information from a given sample it is essential to maximize the volume of an undamaged crystal that can be irradiated with X-rays and contribute to the diffraction signal and maximize PE escape. The optimum spacing is of the order of the PE penetration depth. Unfortunately, using current technology it is not possible to fabricate such an array, which requires etching the lens shape perpendicular to the surface of a silicon wafer to a depth of the order of 100 µm. An alternative solution is proposed to fabricate an array of 4–10 lenses separated by ∼25 µm and to cover the regions between the lenses by moving the array horizontally in steps of ∼5 µm. If the height is greater than that of the line focus its height can be moved vertically as necessary to cover the remaining fresh areas.

6. Summary and conclusions

In summary, we find that the use of a submicrometre line-focus lens provides a radiation-damage mitigation factor of greater than 4, *i.e.* the damage in the irradiated region on focusing is less than 25% of that in the large-beam case with the same X-ray dose, diffraction signal and damaged crystal volume. This effect is explained as a separation of the damage in space between the region of the diffraction signal and PE damage outside that region, as first suggested by Nave & Hill (2005).

A vertical line focus has several advantages. It most efficiently directs the emitted PEs outside the irradiated region,

minimizing damage and the degradation of the diffraction signal. Also, the line-focus beam more efficiently utilizes the crystal volume. By horizontally stepping a single or an array of line beams by an appropriate distance of the order of the PE penetration depth, a large volume of a crystal can be exposed under mitigation conditions. In principle, this approach allows four times more diffraction information to be collected from the crystal compared with the large-beam case. The line-focus PE damage distribution is in only the polarization direction, allowing an accurate measurement of its spatial dependence for the first time. This permitted a comparison with the *CASINO* program (Drouin *et al.*, 2007), exposing inadequacy in the theoretical foundation of the program (see Fig. 3). The measured spatial damage varies monotonically without any peak (Fig. 3).

Finally, we have shown that submicrometre line focusing can be used to collect high-quality atomic resolution data from protein crystals with significantly reduced radiation damage. This approach will be very useful in macromolecular crystallography, particularly with radiation-sensitive macromolecular crystals such as membrane proteins and macromolecular assemblies, as discussed in §1. Our experiments suggest that it is feasible, although technically challenging, to fabricate the arrays of lenses and to align them.

The authors wish to thank the members of the Structural Biology Center at Argonne National Laboratory for their help with data collection on the 19-ID beamline, Kenneth Thompson and Jim Greenwell at the University of Washington Physics Shop for helping with the design and construction of the apparatus and Yizhak Yacoby from Hebrew University for valuable discussions. This work was supported by the National Science Foundation (NSF) under Grant No. 0650547 and by the US Department of Energy (DOE), Office of Biological and Environmental Research under contract DE-AC02-06CH11357. The lenses were fabricated in part at the Brookhaven National Laboratory CFN supported by the US DOE, Office of Basic Energy Sciences under Contract No. DE-AC02-98CH10886 and in part at the Cornell CNF, a member of the NNIN, supported by the NSF.

References

Afonine, P. V., Grosse-Kunstleve, R. W., Echols, N., Headd, J. J., Moriarty, N. W., Mustyakimov, M., Terwilliger, T. C., Urzhumtsev, A., Zwart, P. H. & Adams, P. D. (2012). *Acta Cryst.* D**68**, 352–367.
Borek, D., Cymborowski, M., Machius, M., Minor, W. & Otwinowski, Z. (2010). *Acta Cryst.* D**66**, 426–436.
Bourenkov, G. P. & Popov, A. N. (2010). *Acta Cryst.* D**66**, 409–419.
Carpentier, P., Royant, A., Weik, M. & Bourgeois, D. (2010). *Structure*, **18**, 1410–1419.
Cianci, M., Helliwell, J. R. & Suzuki, A. (2008). *Acta Cryst.* D**64**, 1196–1209.
Dauter, Z., Dauter, M., de La Fortelle, E., Bricogne, G. & Sheldrick, G. M. (1999). *J. Mol. Biol.* **289**, 83–92.
De la Mora, E., Carmichael, I. & Garman, E. F. (2011). *J. Synchrotron Rad.* **18**, 346–357.
Drouin, D., Couture, A. R., Joly, D., Tastet, X., Aimez, V. & Gauvin, R. (2007). *Scanning*, **29**, 92–101.
Emsley, P. & Cowtan, K. (2004). *Acta Cryst.* D**60**, 2126–2132.
Evans-Lutterodt, K., Ablett, J., Stein, A., Kao, C.-C., Tennant, D., Klemens, F., Taylor, A., Jacobsen, C., Gammel, P., Huggins, H., Bogart, G., Ustin, S. & Ocola, L. (2003). *Opt. Express*, **11**, 919–926.
Finfrock, Y. Z., Stern, E. A., Yacoby, Y., Alkire, R. W., Evans-Lutterodt, K., Stein, A., Isakovic, A. F., Kas, J. J. & Joachimiak, A. (2010). *Acta Cryst.* D**66**, 1287–1294.
Garman, E. F. (2010). *Acta Cryst.* D**66**, 339–351.
Garman, E. F. & Weik, M. (2011). *J. Synchrotron Rad.* **18**, 313–317.
Henderson, R. (1990). *Proc. R. Soc. Lond. B Biol. Sci.* **241**, 6–8.
Holton, J. M. (2009). *J. Synchrotron Rad.* **16**, 133–142.
Hovington, P. & Drouin, D. (1997). *Scanning*, **19**, 1–14.
Joy, D. C. & Luo, S. (1989). *Scanning*, **11**, 176–180.
Kmetko, J., Husseini, N. S., Naides, M., Kalinin, Y. & Thorne, R. E. (2006). *Acta Cryst.* D**62**, 1030–1038.
Kmetko, J., Warkentin, M., Englich, U. & Thorne, R. E. (2011). *Acta Cryst.* D**67**, 881–893.
Minor, W., Cymborowski, M., Otwinowski, Z. & Chruszcz, M. (2006). *Acta Cryst.* D**62**, 859–866.
Nave, C. & Hill, M. A. (2005). *J. Synchrotron Rad.* **12**, 299–303.
Paithankar, K. S. & Garman, E. F. (2010). *Acta Cryst.* D**66**, 381–388.
Petrova, T., Ginell, S., Mitschler, A., Kim, Y., Lunin, V. Y., Joachimiak, G., Cousido-Siah, A., Hazemann, I., Podjarny, A., Lazarski, K. & Joachimiak, A. (2010). *Acta Cryst.* D**66**, 1075–1091.
Rosenbaum, G. *et al.* (2006). *J. Synchrotron Rad.* **13**, 30–45.
Salvat, F., Jablonski, A. & Powell, C. J. (2005). *Comput. Phys. Commun.* **165**, 157–190.
Sanishvili, R., Yoder, D. W., Pothineni, S. B., Rosenbaum, G., Xu, S., Vogt, S., Stepanov, S., Makarov, O. A., Corcoran, S., Benn, R., Nagarajan, V., Smith, J. L. & Fischetti, R. F. (2011). *Proc. Natl Acad. Sci. USA*, **108**, 6127–6132.
Shimizu, N., Hirata, K., Hasegawa, K., Ueno, G. & Yamamoto, M. (2007). *J. Synchrotron Rad.* **14**, 4–10.
Sliz, P., Harrison, S. C. & Rosenbaum, G. (2003). *Structure*, **11**, 13–19.
Stern, E. A., Yacoby, Y., Seidler, G. T., Nagle, K. P., Prange, M. P., Sorini, A. P., Rehr, J. J. & Joachimiak, A. (2009). *Acta Cryst.* D**65**, 366–374.
Teng, T.-Y. & Moffat, K. (2002). *J. Synchrotron Rad.* **9**, 198–201.
Wang, J., Dauter, M., Alkire, R., Joachimiak, A. & Dauter, Z. (2007). *Acta Cryst.* D**63**, 1254–1268.
Warkentin, M., Badeau, R., Hopkins, J. & Thorne, R. E. (2011). *Acta Cryst.* D**67**, 792–803.
Warkentin, M., Hopkins, J. B., Badeau, R., Mulichak, A. M., Keefe, L. J., Thorne, R. E.G (2013). *J. Synchrotron Radiat.* **20**, 7–13.
Weik, M., Ravelli, R. B. G., Kryger, G., McSweeney, S., Raves, M. L., Harel, M., Gros, P., Silman, I., Kroon, J. & Sussman, J. L. (2000). *Proc. Natl Acad. Sci. USA*, **97**, 623–628.